nature communications

Article

https://doi.org/10.1038/s41467-026-74223-5

Microbubble elevator induced buoyancy oscillations of reacting droplets

Received: 20 January 2026

Accepted: 21 May 2026

Published online: 11 July 2026

Check for updates

Fattahi Kobra[1,6], Boubakar Sanogo[1,6], Qiuyun Lu[1,6], Yuqi Li[2,6], Ben Bin Xu[3], Detlef Lohse[4,5] ✉, Daosheng Deng[2] ✉ & Xuehua Zhang[1,4] ✉

Autonomous droplet oscillations are intriguing and provide a strong inspiration for the development of active soft matter. However, they are often limited by their reliance on external gradients and slow transport. Here, we demonstrate a propulsion mechanism driven by confined interfacial reactions: the hydrogen microbubble elevator. We show that hydrogen evolution within a liquid organic hydrogen carrier (LOHC) droplet and the resulting bubble pinch off modulate the droplet's effective density, inducing periodic rising and sinking cycles in a stratified fluid. These droplets reach peak velocities of up to 25 mm/s over 2.5 cm trajectories - three orders of magnitude faster than typical Marangoni-driven bouncing - and sustain robust oscillatory motion for up to 25 minutes. The oscillation period and amplitude are programmable through the reaction kinetics, with motion persisting until the bubble-to-droplet size ratio exceeds a critical threshold. With a force balance model, we can quantitatively explain the experimental results and the interplay between gas evolution rates and hydrodynamic forces.

Active soft matter is defined by the ability to transduce free energy into mechanical work, creating systems that operate far from equilibrium[1–4]. Droplets have emerged as a canonical model for such behavior because they combine deformability with spatial confinement, offering a minimal analog to living cells, where chemical fluxes directly couple to mechanical response[5–7]. A central paradigm in this field is the use of interfacial gradients - chemical, thermal, or solutal - to drive motion via, Marangoni stresses, diffusiophoresis, or other effects[8–12]. While these gradients generate complex trajectories, such as the periodic bouncing in stratified liquids[13,14], they face a fundamental constraint: propulsion inevitably decays as diffusive and advective mixing erode the driving gradients[15,16].

To circumvent these diffusive limitations, a distinct propulsion strategy exploits the violent events in phase transitions. Localized heating or optical excitation can nucleate vapor microbubbles[17–19], which subsequently collapse to deliver impulsive forces. Unlike viscous Marangoni flows, these discrete events sustain high-energy oscillations as long as the external driving force persists[20–22]. In the context of rigid micromotors, such inertial impulses can yield velocities approaching 1 m/s[23], while chemical decomposition strategies (such as O_2 generation from H_2O_2) offer a continuous alternative, propelling motors at speeds near 10 μm/s[24]. However, integrating this bubble dynamics into soft, autonomous microdroplets remains a challenge.

Bridging the gap between soft confinement and impulsive propulsion requires exploiting the interfacial kinetics[25]. Reactions confined to the droplet surface can proceed up to a million times faster than in the bulk, accelerated by the synergy of high surface-to-volume ratios and advective transport[26–28]. Within this framework, liquid organic hydrogen carriers (LOHCs) have emerged as a pivotal material system. While primarily designed for reversible hydrogen storage[29,30], LOHC droplets act as autonomous micro-reactors where rapid

[1]Department of Chemical and Materials Engineering, University of Alberta, Edmonton, AB, Canada. [2]Department of Aeronautics and Astronautics & College of Intelligent Robotics and Advanced Manufacturing, Fudan University, Shanghai, China. [3]School of Engineering, Physics and Mathematics, Northumbria University, Newcastle upon Tyne, UK. [4]Physics of Fluids Group, Max Planck Center Twente for Complex Fluid Dynamics, University of Twente, Enschede, The Netherlands. [5]Max Planck Institute for Dynamics and Self-Organization, Göttingen, Germany. [6]These authors contributed equally: Fattahi Kobra, Boubakar Sanogo, Qiuyun Lu, Yuqi Li. ✉e-mail: d.lohse@utwente.nl; dsdeng@fudan.edu.cn; xuehua.zhang@ualberta.ca

interfacial dehydrogenation drives sustained gas production[31,32]. This coupling turns the droplet into a highly efficient engine, merging the interfacial reaction with the dynamics of bubble-driven propulsion[4,33].

Here, we demonstrate that LOHC droplets function as autonomous buoyancy oscillators, driven by confined liquid-liquid interfacial hydrogen evolution. In contrast to rigid micromotors that rely on bubble expulsion for impulsive thrust, our system utilizes internal bubble growth and detachment to periodically modulate the droplet's effective density providing a new propulsive system that operates over a long distance for a long duration. This mechanism induces vertical oscillations in a stratified alkaline medium, achieving peak ascent speeds of 25 mm/s, orders of magnitude faster than Marangoni-driven bouncing[9,13,15]. We show that these dynamics are highly robust, sustaining up to 130 cycles over 25 minutes, with both frequency and stroke length programmable via the reaction rate. Finally, we identify a critical stability limit: oscillations persist only while the bubble-to-droplet size ratio remains below a threshold, beyond which the droplet rises permanently to the free surface. These findings establish gas-evolution interfacial reaction modulation as a potent mechanism for vertical transport in soft active matter.

Results

Oscillatory motion of a reactive droplet

A polymethylhydrosiloxane (PMH) droplet of radius $R_{D,0}$ = 1.54 mm placed in a stratified acetone-NaOH solution at a bulk concentration C_N = 0.5 M sinks under gravity until it stabilizes at its equilibrium position $Z_0 = 0$, where it is neutrally buoyant. After an incubation time of ≈ 25 s, H_2 bubbles nucleate inside the droplet through the dehydrogenation reaction of PMH (Fig. S1A)[34,35]. Bubbles emerge near the base of the droplet and migrate to its apex, where they coalesce with others (Fig. 1A, B). As the bubble further grows by the ongoing chemical reaction, the effective buoyancy of the droplet-bubble compound increases, driving it upward to a peak position $Z \approx 7$ mm within ~ 7.5 s. At this instant, the bubble detaches, and the sudden loss of buoyant volume causes the droplet to sink back to Z_0 in less than 2 s. This rise-sink sequence then repeats over 77 cycles in this particular case, producing a robust oscillatory motion of amplitude $\mathcal{A}(i) = Z(i) - Z_0$

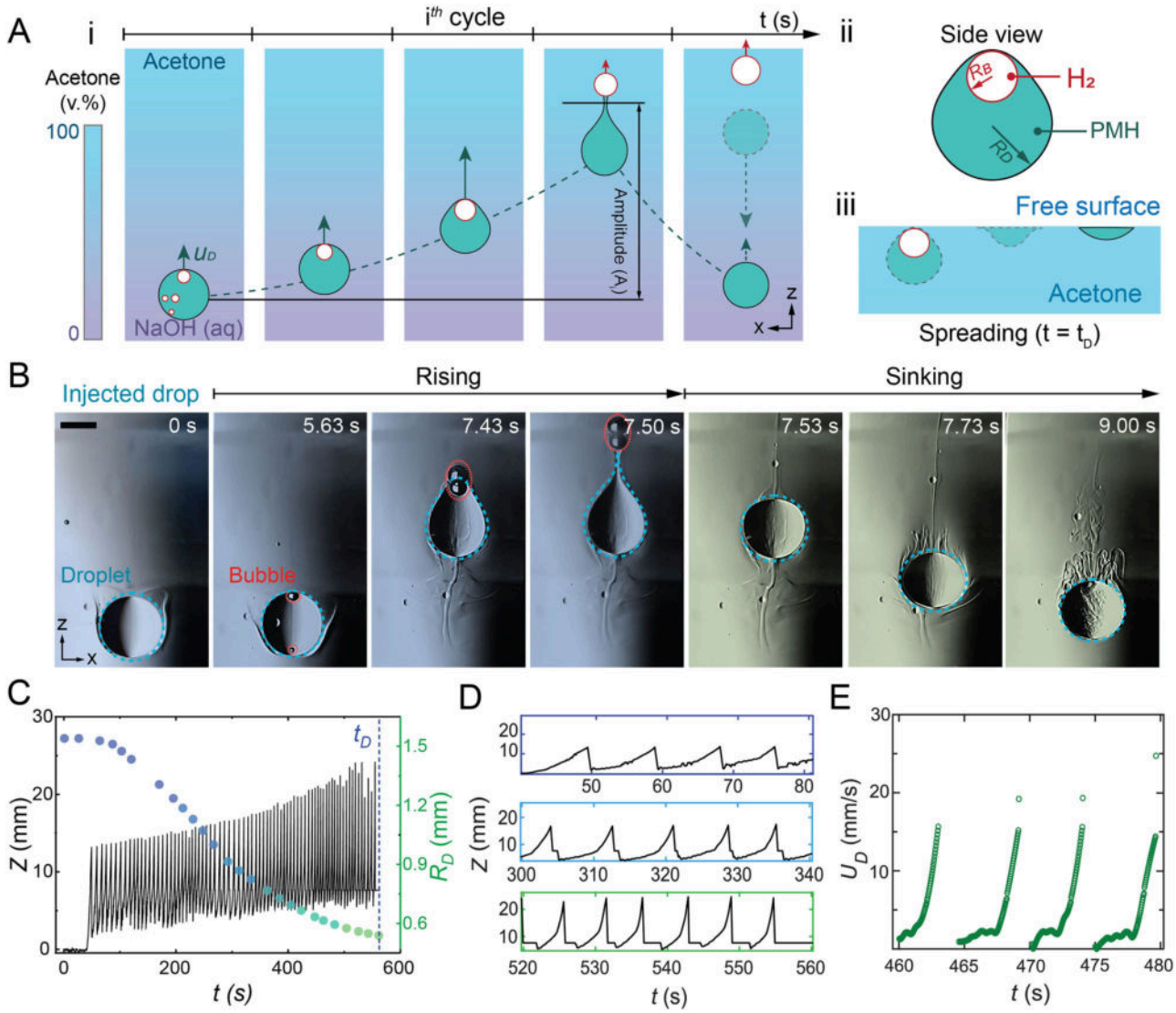

Fig. 1 | Oscillatory motion of a reactive PMH droplet in a stratified acetone-NaOH medium. A Schematic illustration of droplet dynamics: (i) rising and sinking, (ii) side view of a droplet-bubble composite, and (iii) terminal spreading at the air-liquid interface. **B** Sequential snapshots of a PMH droplet in a stratified acetone-NaOH solution (C_N = 0.5 M), showing a complete rise-sink cycle. Scale bar: 2 mm. **C** Time evolution of droplet bouncing amplitude (Z) and droplet size (R_D). The color transition from blue to green in R_D reflects the temporal progression of the bouncing dynamics. **D** Bouncing amplitude during representative early, middle, and late stages (zoomed-in views). **E** Maximum rising velocity measured during the late bouncing stages.

https://doi.org/10.1038/s41467-026-74223-5

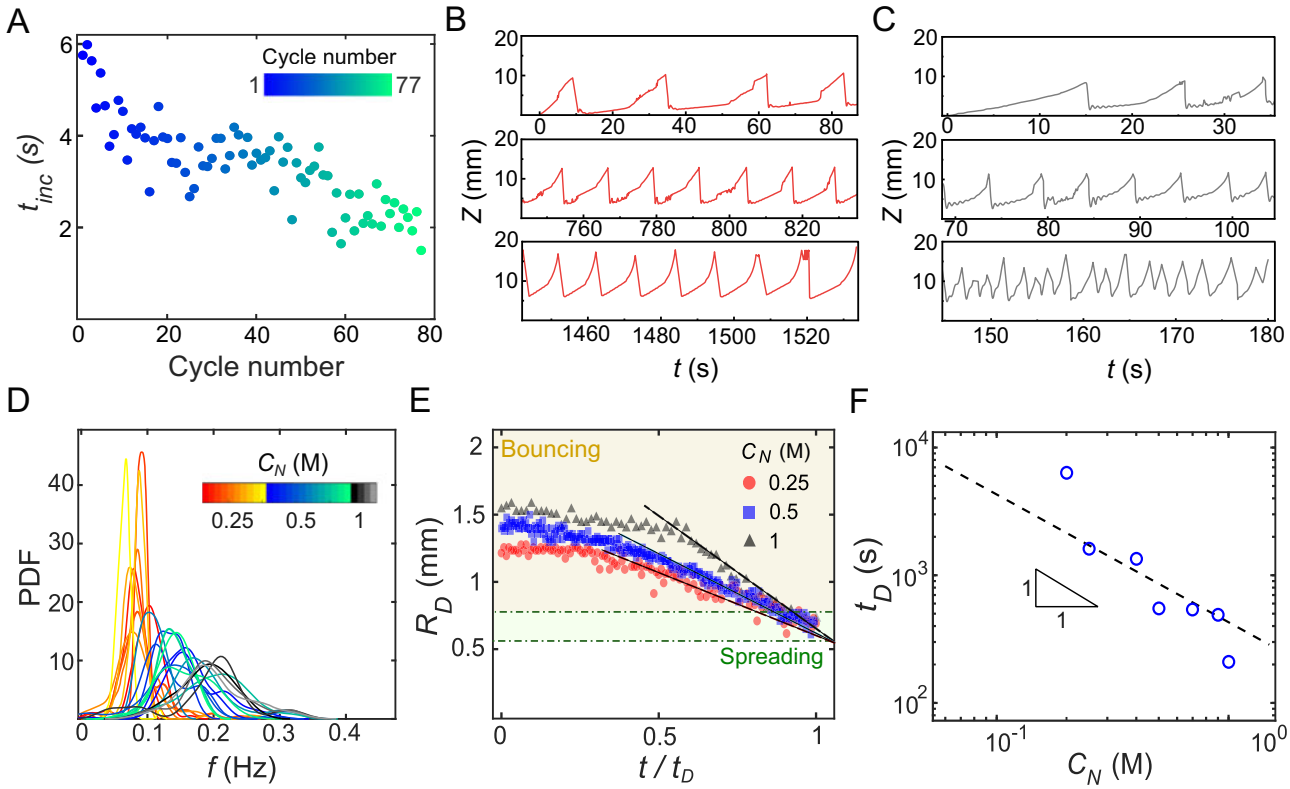

Fig. 2 | Effect of NaOH concentration on the bubble-driven oscillatory dynamics. A Incubation time at the resting position prior to the onset of bubble-driven motion (C_N = 0.5 M). Representative oscillation amplitude for: **B** C_N = 0.25 M and (**C**) C_N = 1 M. **D** Dependence of the mean oscillation frequency and total number of oscillation cycles on C_N. **E** Droplet radius evolution $R_D(t)$ highlighting concentration-dependent shrinkage dynamics. **F** The droplet lifetime at different hydroxide concentrations.

(Supplementary Video 1), where i is the cycle number. Eventually, during the final rise, the last rising bubble entrains the now much smaller droplet to the surface, where it detaches and spreads across the liquid-air interface of the bath (Fig. 1A(iii) and Supplementary Video 2).

Figure 1C tracks the vertical displacement of the droplet, showing a progressive increase in oscillation amplitude $\mathcal{A}$ as the droplet becomes gradually smaller due to the loss of PMH. The amplitude grows from $\mathcal{A}(1)$ = 11 mm to $\mathcal{A}(77)$ = 20 mm, mainly due to higher rise positions, while the return level remains close to $Z \approx Z_0$. In parallel, the incubation time shortens from ≈ 6 s to 2 s, which indicates that the droplet spends progressively less time at rest before each ascent (Fig. 2A), reflecting its smaller size. This results in an increase in the bouncing frequency from ≈ 0.1 Hz in the early cycles to ≈ 0.16 Hz in the later stages (Fig. 1D). These trends reflect two coupled effects, namely, as already mentioned, (i) the gradual reduction of the droplet radius R_D, shrinking nearly 3-fold due to progressive depletion of the PMH droplet (Fig. 1C) - and (ii) variations in bubble growth dynamics as will be discussed below. As the droplet becomes smaller, the relative buoyancy of each bubble as compared to that of the droplet becomes larger, triggering earlier departures from the resting position and driving the droplet to increasingly higher rise positions. In contrast, Marangoni-driven bouncing shows the opposite trend: droplets progressively sink deeper and return to the same top position[15].

The bubble-carrying droplet exhibits a sharp increase in velocity when crossing from the water-rich region to the acetone-rich region, with the velocity increasing by nearly 2-fold. The maximum rising velocity U_D also evolves over time, increasing from about 4 mm/s in the initial jumps to 25 mm/s after tens of cycles, because of the progressive shrinkage of the droplet (Fig. 1E). A comparable acceleration was reported by Li et al.[15] for sinking trans-anethole droplets in stratified water-ethanol solutions, where it was attributed to mixing induced by repeated oscillations. Here, the trend originates from the coupled dynamics of droplet shrinkage and bubble growth dynamics.

The essential driver of the oscillatory behavior is the bubble formation inside the droplet by interfacial reaction, where the buoyancy generated by the bubble initiates the periodic rise-sink motion. Acetone is needed for establishing a stratified density profile so that the droplet can suspend, and also for reducing the interfacial tension between the droplet and the surrounding at a high Z position. In addition to acetone, other liquids with low density, miscibility in water, and non-reactivity with PMH, such as acetonitrile, could also be used for stratification. We also performed control experiments in a stratified acetone-water solution under identical conditions but without NaOH, or with a low concentration (0.15 M). In these cases, surface tension gradients developed, yet no bubbles were generated. The droplet either sank continuously or levitated at an intermediate position (Fig. S2). These observations exclude Marangoni stresses as the origin of the oscillatory motion. Therefore, the oscillatory bouncing motion is primarily driven by buoyancy force due to the produced gas bubble.

Controlling droplet oscillation via reaction rates

Since the oscillatory motion of the droplet arises from the hydrogen bubble formation and growth inside the PMH droplet, the oscillation characteristics should be tunable through the reaction rate. To test this idea, we systematically varied the alkalinity of the surrounding solution, using bulk NaOH concentrations C_N between 0.1 M and 1 M. Across this range, we studied more than 50 droplets with initial radii between 0.7 mm and 2.0 mm, which underwent 25–130 oscillation cycles and exhibited lifetimes t_D (duration from the initial incubation to surface spreading) between 145 s and 1500 s.

Representative oscillations at C_N = 0.25 M and 1 M are shown in Fig. 2B and C. The maximum oscillation amplitude is reduced relative

to C_N = 0.5 M, by ≈ 35% at 0.25 M and ≈ 50% at 1 M, consistent with a lower upper turning point prior to the sinking phase. An upward shifting in the position of the settled droplet was observed in all three concentrations of NaOH solution (Fig. S10). Such gradual rise in the settling position of the droplet may be attributed to the local mixing of the stratified surrounding solution by the reacting droplet, which shifts the density match point upward. Moreover, higher C_N yields faster oscillations, with the average frequency rising from ≈ 0.1 Hz to 0.2 Hz (Fig. 2D), while the total number of bounces decreases from 130 to 25. These trends reveal a trade-off between enhanced jump dynamics and overall droplet lifetime. Over the concentration range explored, C_N = 0.5 M yields both the largest amplitudes and the most temporally regular dynamics, with minimal cycle-to-cycle variations in amplitude and period.

The underlying mechanism of the NaOH concentration effect is captured by the interfacial reaction driving H_2 bubbles nucleation and growth. Following Dyett et al.[36], the local dissolved H_2 concentration at the droplet interface can be approximated as: $dC_S/dt = 3k \cdot [PMH]_D \cdot [OH^-]_S(t) \cdot R_D^{-1}(t)$ (Supplementary Section 6), where $[PMH]_D$ and $[OH^-]_S$ are the concentrations of PMH (droplet phase) and hydroxide ions (in the surrounding solution), respectively. As C_N increases, droplets are exposed to higher $[OH^-]_S$, which accelerates H_2 production rate and promotes faster bubble growth, shortens incubation times, and reduces growth periods. Such modifications account for the observed increase in bouncing frequency and the concurrent reduction of oscillation lifetime, analogous to observations with swimming microrobots, where increasing fuel concentration similarly accelerates bubble-driven propulsion[37].

Because H_2 production drives repeated bubble detachment, which removes a small amount of droplet liquid each cycle, the oscillatory dynamics are intrinsically coupled to droplet shrinkage. Regardless of C_N, $R_D(t)$ exhibits two regimes: an initial slow decrease followed by a faster, nearly linear decay that starts at $t \approx 1/2\, t_D$ (Fig. 2E). The onset of this accelerated shrinkage coincides with an increase in bouncing frequency, which indicate a direct coupling between oscillatory dynamics and material loss. As C_N increases, the slope of the late-stage decay becomes steeper, reflecting more rapid droplet depletion at higher hydroxide concentration. Consequently, the droplet lifetime decreases systematically with C_N, displaying $t_D \sim C_N^{-1}$ (Fig. 2F). It is noteworthy that rapid bouncing at C_N = 1 M causes the fragmentation of the primary droplet and produces satellite droplets that are not captured by R_D.

As the oscillatory motion proceeds and the droplet continues to shrink, the bubble occupies an increasingly large fraction of its interior. During the early cycles, buoyancy stretches the droplet and capillary bridges eventually enable bubble detachment. However, once the droplet falls below a critical size, the bubble can no longer pinch-off. Instead, the bubble entrains the entire droplet and the two rise together to the free surface (Supplementary Video 2). In this final regime, no capillary neck forms (Fig. S8), and entrainment occurs when the net buoyant force of the composite becomes positive:

$$(\rho_{str} - \rho_D)R_D^3 + \rho_{str} R_B^3 \geq 0. \quad (1)$$

Here, R_B is the bubble radius, ρ_{str} and ρ_D are the densities of the stratified acetone-rich layer and droplet, respectively. This condition defines a critical bubble-to-droplet radius ratio:

$$\beta^* \equiv \frac{R_B^*}{R_D} = \left(\frac{\rho_D - \rho_{str}}{\rho_{str}}\right)^{1/3}, \quad (2)$$

with R_B^* the maximum bubble radius on the verge of detachment. The calculated β^* ≈ 0.57 is in good agreement with the experimental threshold of ~ 0.59 ± 0.01. Additionally, the corresponding final droplet radii (0.5–0.8 mm) are consistent with the measurements in the final cycles (Fig. 2E), confirming that entrainment is controlled primarily by the bubble-to-droplet radius ratio.

Dynamics of internal bubble growth

To characterize the driving force behind the droplet oscillations for C_N = 0.5 M, we tracked the temporal evolution of the bubble radius, $R_B(t)$ (Fig. 3A). Over the droplet lifetime (t_D = 560 s), $R_B(t)$ displays quasi-periodic growth, reaching its maximum value immediately before bubble detachment. After each detachment, R_B abruptly decreases to very small but non-zero values, as fresh nuclei form within the droplet almost instantaneously.

Close inspection of each oscillation cycle shows that both the maximum bubble radius at detachment (R_B^*) and the growth process duration depend on the stage of the droplet's lifetime. Early in the cycles, bubbles detach at $R_B^* \approx 0.53$ mm, a value that decreases to 0.28 mm in the final oscillation (Fig. 3B). In parallel, the growth duration shortens from ~ 9 s to 3 s, consistent with the reduction in the droplet oscillation period from ~ 10 s to 2.5 s. Together, these trends demonstrate that the progressive acceleration of the droplet's oscillations directly reflects the evolving dynamics of bubble growth and detachment.

The bubble detachment occurs progressively higher in the stratified system, with each released bubble coated by a thin PMH layer (Fig. 3C). The detachment first takes place near the transition between the water-rich and acetone-rich layers, then shifts upward as the droplet reaches regions of lower density and reduced interfacial tension. The detachment process can be understood from the competition between the buoyancy force, which drives the bubble upward, and the capillary force, which resists the bubble escape from the droplet (Fig. S8). This balance is captured by the Bond number:

$$Bo(Z) = \frac{\rho_D\, g\, R_B^2}{\sigma(Z)} \quad (3)$$

where g is the gravitational acceleration and $\sigma(Z)$ the interfacial tension between the droplet and the surrounding solution. Within each oscillation cycle, Bo increases as the bubble grows and capillary confinement progressively weakens as the droplet rises into the acetone-rich region. Using the small interfacial tension $\sigma(Z) \approx 0.4$ mN/m measured at the interface between the droplet and the surrounding acetone-NaOH solution, bubble detachment consistently occurs for $Bo > 1$, where buoyancy overcomes capillary confinement (Fig. 3D). However, the detachment threshold decreases systematically over successive cycles: from $Bo \approx 7$ in the earliest cycles to $Bo \approx 4.5$ in mid cycles and eventually $Bo \approx 2$ in the final stages. This decline directly reflects the progressive reduction of the maximum bubble radius at detachment R_B^*.

The time-dependent bubble-to-droplet radius ratio $\beta(t) \equiv R_B(t)/R_D(t)$ overall increases over successive cycles because the droplet shrinks faster than the bubble size decreases. This ratio reflects the gas fraction of the droplet-bubble compound, which directly influences its effective density and buoyancy. As the bubble occupies a larger fraction of the compound's volume, the buoyancy during a cycle grows relative to hydrodynamic drag. This shifting force balance explains the progressively faster rising velocity observed in Fig. 1E.

To understand these trends, it is essential to analyze the bubble growth dynamics. Previous studies with reactive surface-bound PMH droplets showed that H_2 bubble growth is diffusion-limited[38], meaning that the chemical reaction is fast enough for mass transport to control the overall dynamics (i.e., large Damköhler number). This is consistent with Dyett and Zhang's[36] observation that the H_2 formation rate scales inversely with microdroplet size, $R_B^{\cdot} \sim R_D^{-1}$. In contrast, bubbles inside our millimeter-scale droplet-bubble compounds grow at a nearly constant rate of $(9.8 \pm 1.1) \times 10^{-2}$ mm/s throughout each cycle (Fig. 3E),

https://doi.org/10.1038/s41467-026-74223-5

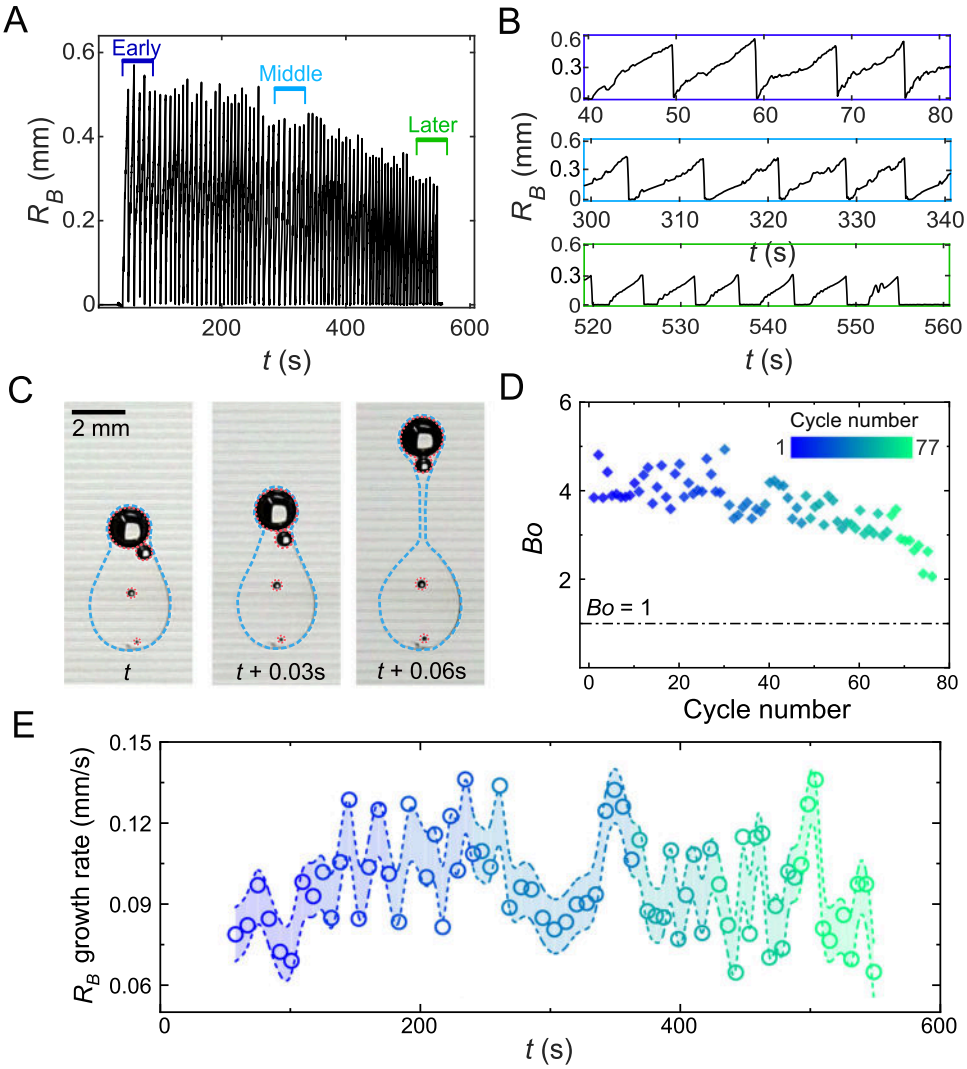

Fig. 3 | Bubble growth and detachment dynamics from the reactive PMH droplet at C_N = 0.5 M. A, **B** Time evolution of bubble size (R_B) within a droplet (R_D = 1.54 mm, C_N = 0.5 M) throughout its lifetime (t_D = 560 s). **C** Sequential snapshots of the bubble detachment process, showing a capillary neck and the release of a bubble coated by a thin PMH layer. Blue contours represent the droplet interface and red circles indicate H_2 bubbles. **D** Bond number (Bo) at the moment of bubble detachment from the PMH droplet for successive oscillation cycles. **E** Bubble growth rate for each oscillation cycle, obtained from the late stage growth before detachment under the assumption of linear evolution. The shading represents the standard deviation obtained from measurements on 10 growing bubbles.

consistent with prior observations that size-dependent growth dynamics vanish at larger droplet scales[32].

Force balance model of the oscillating droplet

To further quantify the bubble-driven oscillations of PMH droplet in the stratified medium with position-dependent density $\rho_{str}(Z)$ (Fig. 4A), we now develop a physical model that couples buoyancy-driven motion, bubble growth, and droplet shrinkage (More details are provided in Supplementary Section 8). Here, the composite droplet-bubble system is characterized by a time-dependent radius $R_{eD}(t) = [R_D^3(t) + R_B^3(t)]^{1/3}$ (Fig. 4B) and an effective density $\rho_{eD}(t) \approx \rho_D R_D^3(t)/[R_D^3(t) + R_B^3(t)]$.

Considering that the compound is subjected to buoyancy force $F_{buo} = -[\rho_{eD}(t) - \rho_{str}(Z(t))]\, V_{eD}(t) g$ and Stokes drag force $F_{drag} = 6\pi\eta_{str} R_{eD}(t) Z^{\cdot}(t)$, the temporal vertical position of the composite is governed by a quasi-steady balance between buoyancy and viscous drag:

$$Z^{\cdot}(t) = \frac{[\rho_{str}(t) - \rho_{eD}(t)]\, V_{eD}(t) g}{6\pi\, \eta_{str}\, R_{eD}(t)}. \quad (4)$$

As the bubble volume increases, the compound becomes lighter ($\rho_{eD} \le \rho_{str}$) and rises ($Z^{\cdot} \ge 0$). When the buoyant force overcomes the capillary confinement that holds the bubble within the droplet, the bubble detaches from the droplet, leading to an abrupt transition to a sinking phase under gravity ($\rho_{eD} \ge \rho_{str}$ and $Z^{\cdot} \le 0$).

Within a single oscillation cycle, the droplet volume remains approximately constant, but the internal H_2 bubble grows through a diffusion-limited interfacial reaction. Therefore, the radius of the bubble-droplet composite R_{eD} increases with reaction time, and the bubble growth rate is described as:

$$R_B^2 R^{\cdot}_B = \alpha(Z) R_{eD}^2,\ \alpha(Z) = \alpha\, C_N (1 + Z/l). \quad (5)$$

Here, R_B is the bubble's radius, $\alpha(Z)$ the reaction rate, with α an effective reaction rate coefficient, C_N the NaOH concentration (assuming the reaction rate for gas production is linearly proportional to this concentration), and l a characteristic vertical length scale that sets the dependence of the reaction rate on position in the stratified medium.

As shown in Fig. 3B, bubble growth accelerates when the composite rises into the less dense, acetone-rich region of the stratified solution due to lower Laplace pressure from the reduced interfacial

https://doi.org/10.1038/s41467-026-74223-5

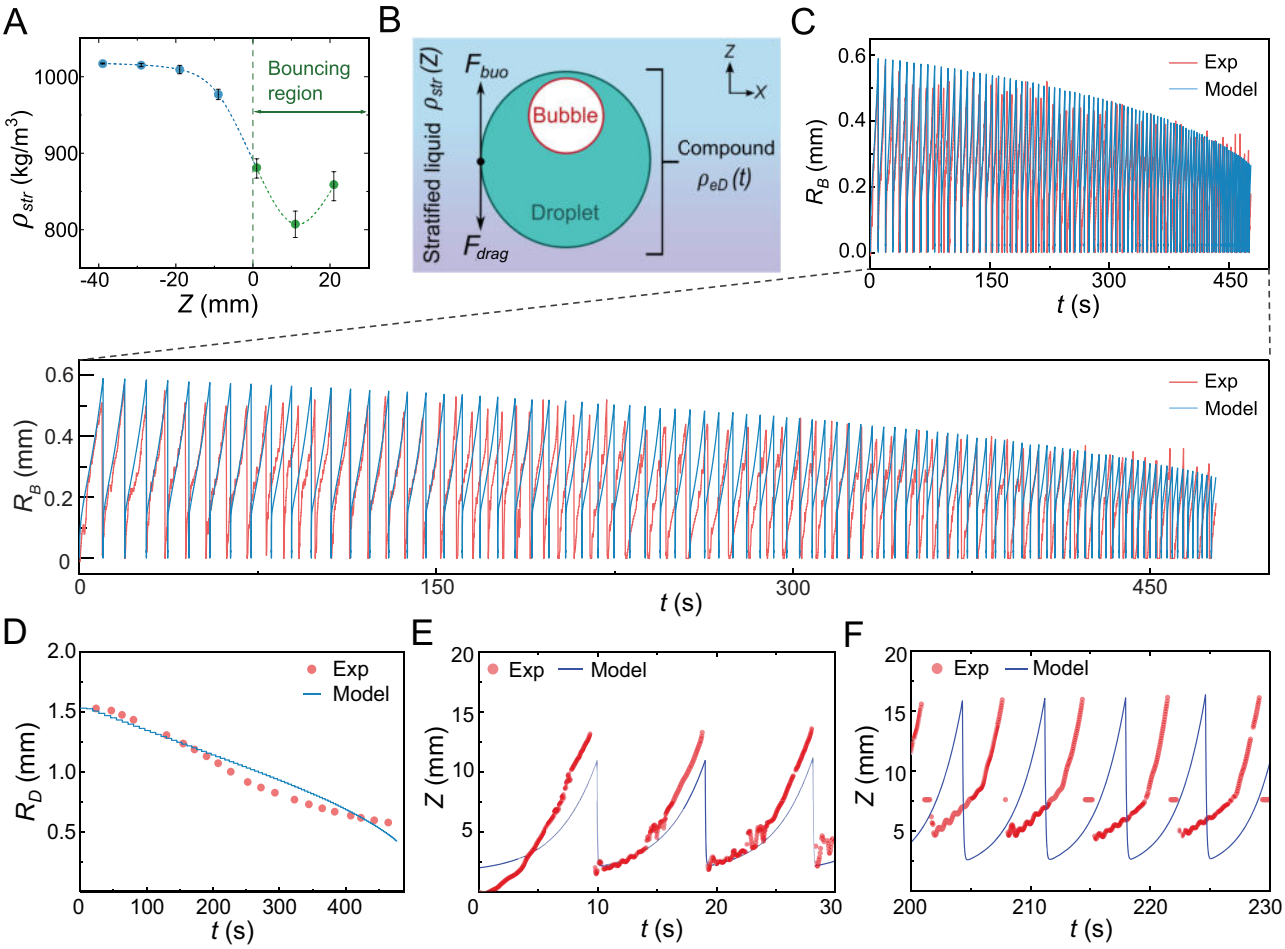

Fig. 4 | Mechanism and modeling of the bouncing droplet. A Measured density profile $\rho_{str}(Z)$ of the stratified acetone-NaOH solution at C_N = 0.5 M. Error bars denote the standard deviation of 3 measurements. The origin $Z = 0$ corresponds to the initial position of the droplet. Based on the measured density profile, the local environment within the active bouncing region spans from a highly acetone-rich phase (~ 94 vol.% acetone at the upper boundary) to a mixed aqueous phase (~ 64 vol.% acetone at the lower boundary). **B** Schematic of the droplet-bubble composite highlighting the dominant forces: buoyancy, F_{buo}, and viscous drag, F_{drag}. **C** Time evolution of the bubble radius R_B for C_N = 0.5 M: red lines represent experiments and blue lines show the corresponding model results. The model parameters are $\alpha = 8.0 \times 10^{-7}$ m/(M · s), and $l = 4.0 \times 10^{-4}$ m, and the dimensionless constant $\gamma = 0.4$. The known material properties were used as listed in Table S2. **D** Time evolution of the droplet radius R_D under the same conditions. Comparison of experimental (symbols) and simulated (lines) vertical trajectories $Z(t)$ for oscillation cycles in the early (**E**) and intermediate (**F**) stages.

tension, despite the lower local concentration of OH^- ions and slower reaction rate in this layer. Bubble detachment occurs when a critical Bond number is exceeded $[Bo(R_B(t^*) = R_B^*) \geq Bo_c]$, thereby resetting the oscillation cycle.

During bubble pinch off from the droplet, the detachment takes the droplet liquid along with it, resulting in the droplet shrinking. Hence, the shrinkage of droplet R_D is modeled as:

$$\frac{4}{3}\pi\left(R_{D,n-1}^3 - R_{D,n}^3\right) = \gamma \frac{R_B^2(t^*)\nu_{str}}{Z^{\cdot}(t^*)} \quad (6)$$

where $R_{D,n}$ is the droplet radius after the n^{th} detachment event, t^* is the detachment time, ν_{str} is the kinematic viscosity of the surrounding solution, and γ is a dimensionless constant. Here, $[\nu_{str}/Z^{\cdot}(t^*)]$ is the boundary layer thickness around the bubble at the moment of detachment.

By numerically solving the coupled system governing the composite motion (Eq. (4)), the bubble growth law (Equation (5)), the droplet shrinkage rule (Equation (6)), and the bubble detachment criterion (Eq. S9), we obtain a dynamical model for the oscillation process. This model yields the time evolution of the bubble radius $R_B(t)$ (Fig. 4C), the droplet radius $R_D(t)$ (Fig. 4D), and the vertical position $Z(t)$ (Figs. 4E, F and S10) all in good agreement with the experimental results during the early and middle stages.

Figure 4E and F shows the simulated vertical motion of representative droplets at two stages of their evolution: an early cycle with $R_D \approx 1.53$ mm (t = 0 − 30 s) and a late cycle with $R_D \approx 1.07$ mm (t = 200 − 230 s). The smaller droplet exhibits a larger oscillation amplitude and a shorter period. These trajectories reflect the general trend of the simulated bouncing throughout the entire process (Fig. S10). As the droplet and bubble shrink, the oscillation amplitude increases while the period continues to decrease. The deviation at the late stage likely stems from the assumption of a constant reaction rate coefficient in the model, whereas in experiments the reaction rate decreases with time due to the gradual consumption of the chemical reactant and the accumulation of the chemical product near the droplet. Moreover, the model reproduces the experimentally observed reduction in droplet lifetime with increasing NaOH concentration (Fig. S10). Despite the complex system, our simple model has a remarkable agreement with the experiments, and reveal the gas-bubble-driven droplet oscillation.

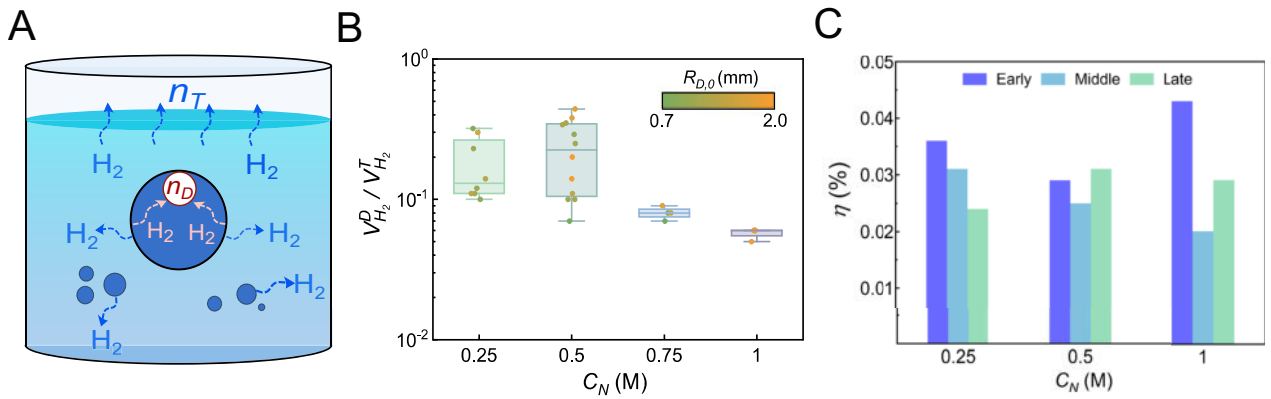

Fig. 5 | Hydrogen generation pathways and energy conversion in bubble-driven droplet oscillations. A Schematic illustration of the two sites of H_2 accumulation: within the droplet and in the surrounding solution. **B** Ratio of H_2 volume originating from the droplet ($V^D_{H_2}$) to the total H_2 volume ($V^T_{H_2}$) at different C_N. Error bars denote the standard deviation obtained from measurements on 4 to 12 reacting droplets, and the horizontal line within each box plot represents the median value. **C** Chemical-to-mechanical energy conversion efficiency (η) of a droplet ($R_{D,0}$ = 1.54 mm). The efficiency is shown for the early, middle, and late stages of the droplet's oscillation cycle.

Notably, our minimal model employs a quasi-steady Stokes drag approximation for conceptual simplicity. The peak ascent velocity (~25 mm/s) extends slightly beyond the strict Stokes regime, where inertial effects play a role. While empirical corrections (e.g., the Schiller-Naumann correction) can be implemented to slightly increase the drag term, we retain Stokes drag as approximation by absorbing those higher-order inertial contributions into the empirically fitted prefactors (α, l, and γ).

Contribution of H_2 production from the bubble elevator

Hydrogen is released at the droplet-water interface and then partitions by diffusion: inward into the PMH droplet, where it nucleates bubbles, and outward into the surrounding aqueous environment. To quantify the relative importance of these pathways, we compared the cumulative H_2 volume contained in in-droplet bubbles over oscillation cycles ($V^D_{H_2}$) with the total H_2 volume accumulated in the container headspace ($V^T_{H_2}$), as illustrated in Fig. 5A. The ratio $V^D_{H2}/V^T_{H_2}$ remains much less than 0.5, showing that a substantial fraction of H_2 produced at the interface ultimately diffuses outward through the surrounding alkaline solution and accumulates in the headspace (Fig. 5B). As C_N increases from 0.25 M to 1 M, the ratio declines by nearly 4-fold, indicating that faster interfacial gas formation further reduces the droplet's fraction of the total collected gas.

These gas ratios reflect droplet confinement coupled with gas transport from the droplet interface. The headspace volume is all the H_2 produced at the interface, including gas that briefly resides in the droplet before diffusing out or detaching, and therefore increases monotonically. The in-drop bubble is a temporary reservoir from oversaturated gas in the droplet's small volume. Mechanistically, the interfacial concentration C_S rises with C_N as mentioned before, steepening the gradient ($C_S - C_\infty$) and enhancing outward diffusion (Fickian transport). In contrast, the principal in-droplet bubble serves as a stabilized sink by bubble growth and detachment, and H_2 retention is limited by the higher-viscosity of the droplet and slower internal transport.

Finally, we compared the chemical energy released per cycle with the mechanical work required to lift the droplet. The chemical input from the reaction enthalpy associated with H_2 formation is on the order of 10^{-3} - 10^{-2} J per cycle, whereas the mechanical output remains 10^{-7} - 10^{-6} J per cycle (Fig. 5C). The resulting chemical-to-mechanical conversion efficiency is therefore very small, $\eta \sim 10^{-4}$, indicating that most of the chemical energy is dissipated rather than converted into work. This low efficiency is consistent with highly dissipative active matter systems in which the majority of input energy is lost to the environment[39–42].

Discussion

In this work, we have introduced the hydrogen microbubble elevator as a distinct mode of active transport, driven by the density modulation of a reacting LOHC droplet. Our mechanism leverages the growth and detachment of microbubbles from controlled interfacial reactions to achieve rapid, vertical oscillations. We show that this process acts as a tunable chemo-mechanical converter, where the oscillation frequency and stroke are governed by the interplay between interfacial reaction kinetics and capillary forces that entrain the microbubble. By providing a physical framework for programmable buoyancy, this work bridges the gap between chemical synthesis and active matter physics. Similar dynamic behavior reported in this work was also observed for other reactive droplet systems, including other LOHCs (e.g., diphenylsilane), miscible blends of LOHCs with other solvents miscible with water, and liquids evolving other types of gases. In future, research is needed to map out the droplet dynamics, bubble behavior, and bulk and interfacial properties for gas-producing droplet reaction in general.

These self-regulating droplets that are coupled with the interfacial reaction kinetics may offer a new platform for autonomous environmental sensing. Specifically, the oscillation frequency and amplitude may potentially serve as a readout for local reactant concentrations (e.g., OH^- gradients) or map the spatial stratification of complex fluid environments without external power. Furthermore, the single droplet reaction provides a model system for understanding the complex droplet motions driven by internal bubble formation, ultimately guiding the design of reacting mixtures for controlled hydrogen production rate on a large scale.

Methods

Preparation of the stratified solution

A vertical stratified acetone-NaOH solution was prepared in a cylindrical glass vessel with an inner diameter of 23 mm and a height of 70 mm (Fig. S1B). First, 35 mL of the alkaline solution (C_N = 0.25 M - 1 M) was carefully introduced at the bottom of the vessel. Subsequently, 15 mL of acetone was added at a controlled flow rate of 11 mL/min using a syringe pump (New Era Infusion One, NE-300). Immediately after injection, the vessel was sealed with a solid rubber stopper and left undisturbed at room temperature for 24 h, allowing acetone to diffuse downward and form a stable density gradient.

Droplet injection

Droplets were released in the acetone-rich top layer of the stratified solution using a 500 μL syringe (Kruss, USA). The syringe was fitted

with needles of two different outer diameters (0.515 and 0.312 mm) to control droplet size ($R_{D,0}$ = 0.7 mm–2 mm). After injection, each droplet descended until reaching an equilibrium position (26 mm below the free liquid surface), which systematically occurred above the density-matching point (ρ_{str} = 1006 kg/m^3), where its net vertical displacement ceased. After a short induction period, H_2 nucleated and grew within the droplet, initiating the characteristic bouncing behavior. Each round of droplet oscillations employed a single stratified binary mixture. Notably, acetone is highly miscible with water but poorly compatible with PMH. Therefore, it remains in the surrounding phase and does not partition into the PMH droplet[43].

Data availability

The data supporting the findings of this study are provided in the Source Data file. Source data are provided with this paper.

References

1. Lohse, D. & Zhang, X. Physicochemical hydrodynamics of droplets out of equilibrium. *Nat. Rev. Phys.* **2**, 426–443 (2020).
2. Palankar, R. Microrobots mop-up nanoplastics. *Nat. Nanotechnol.* **17**, 821 (2022).
3. Feng, R., He, Y., Feng, S. & Li, S. Impulsive actuation for soft robots. *npj Robot.* **3**, 27 (2025).
4. Lu, Q., Sanogo, B., Kumar, T., Xu, B. B. & Zhang, X. Recent advances in reactive microdroplets for clean water and energy. *Adv. Mater.* **37**, e09486 (2025).
5. Pizarro, A. D., Berli, C. L. A., Soler-Illia, G. J. A. A. & Bellino, M. G. Droplets in underlying chemical communication recreate cell interaction behaviors. *Nat. Commun.* **13**, 3047 (2022).
6. Saleh, O. A., Wilken, S., Squires, T. M. & Liedl, T. Vacuole dynamics and popping-based motility in liquid droplets of DNA. *Nat. Commun.* **14**, 3574 (2023).
7. Tomohara, K., Minagawa, Y. & Noji, H. Artificial cells with all-aqueous droplet-in-droplet structures for spatially separated transcription and translation. *Nat. Commun.* **16**, 627 (2025).
8. Frank, B. D. et al. Reversible morphology-resolved chemotactic actuation and motion of Janus emulsion droplets. *Nat. Commun.* **13**, 2562 (2022).
9. Li, Y., Diddens, C., Prosperetti, A. & Lohse, D. Marangoni instability of a drop in a stably stratified liquid. *Phys. Rev. Lett.* **126**, 124502 (2021).
10. Jin, C., Krüger, C. & Maass, C. C. Chemotaxis and autochemotaxis of self-propelling droplet swimmers. *Proc. Natl. Acad. Sci.* **114**, 5089–5094 (2017).
11. Banerjee, A. & Squires, T. M. Long-range, selective, on-demand suspension interactions: Combining and triggering soluto-inertial beacons. *Sci. Adv.* **5**, eaax1893 (2019).
12. Dreyfus, R. et al. Microscopic artificial swimmers. *Nature* **437**, 862–865 (2005).
13. Meijer, J. G., Li, Y., Diddens, C. & Lohse, D. On the rising and sinking motion of bouncing oil drops in strongly stratified liquids. *J. Fluid Mech.* **966**, A14 (2023).
14. Herrada, M. A., Montanero, J. M. & Carrión, L. Dynamics of a silicone oil drop submerged in a stratified ethanol-water bath. *Phys. Rev. E* **108**, 065104 (2023).
15. Li, Y. et al. Bouncing oil droplet in a stratified liquid and its sudden death. *Phys. Rev. Lett.* **122**, 154502 (2019).
16. Sastre, J. et al. Size control and oscillations of active droplets in synthetic cells. *Nat. Commun.* **16**, 2003 (2025).
17. Xu, L., Mou, F., Gong, H., Luo, M. & Guan, J. Light-driven micro/nanomotors: From fundamentals to applications. *Chem. Soc. Rev.* **46**, 6905–6926 (2017).
18. Lohse, D. Bubble puzzles: From fundamentals to applications. *Phys. Rev. Fluids* **3**, 110504 (2018).
19. Wang, F. et al. Plasmonic bubbles: From fundamentals to applications. *Adv. Funct. Mater.* **34**, 2403606 (2024).
20. Sangani, A. S., Zhang, D. Z. & Prosperetti, A. The added mass, basset, and viscous drag coefficients in nondilute bubbly liquids undergoing small amplitude oscillatory motion. *Phys. Fluids A: Fluid Dyn.* **3**, 2955–2970 (1991).
21. Prosperetti, A., Yuan, H. & Yin, Z. Growth and collapse of a vapor bubble under impulsive heating. In *ASME 2001 International Mechanical Engineering Congress and Exposition*, 43–50 (American Society of Mechanical Engineers, United States, 2001).
22. Hu, M. et al. 3D periodic orbiting of a photothermal bubble. *Phys. Rev. Lett.* **134**, 104004 (2025).
23. Zeng, B. et al. Photothermal cavitation-driven micromotor to penetrate cell membrane. *J. Am. Chem. Soc.* **147**, 8906–8916 (2025).
24. Jang, B. et al. Catalytically propelled micro and nanoswimmers. *Small Sci.* **3**, 2300076 (2023).
25. Shah, P. R., Nery-Azevedo, R., Abdel-Fattah, A. & Squires, T. M. Zwitterion gradients drive colloidal migration. *Langmuir* **41**, 22059–22066 (2025).
26. Jia, M.-Y., Zhou, Y.-W., Yang, J.-L., Liu, Q. & Cai, Z.-F. Catalyst-free Ullmann coupling in aqueous microdroplets. *Nat. Commun.* **16**, 7453 (2025).
27. Zhao, L. et al. Sprayed water microdroplets containing dissolved pyridine spontaneously generate pyridyl anions. *Proc. Natl. Acad. Sci.* **119**, e2200991119 (2022).
28. Wei, Z., Li, Y., Cooks, R. G. & Yan, X. Accelerated reaction kinetics in microdroplets: Overview and recent developments. *Annu. Rev. Phys. Chem.* **71**, 31–51 (2020).
29. Valentini, F., Marrocchi, A. & Vaccaro, L. Liquid organic hydrogen carriers (LOHCs) as H source for bio derived fuels and additives production. *Adv. Energy Mater.* **12**, 2103362 (2022).
30. Zhou, M., Miao, Y., Gu, Y. & Xie, Y. Recent advances in reversible liquid organic hydrogen carrier systems: From hydrogen carriers to catalysts. *Adv. Mater.* **36**, 2311355 (2024).
31. Sanogo, B., Dogra, P., Kalita, K. & Zhang, X. Surfactant-mediated interfacial hydrogen evolution reaction. *ACS Appl. Mater. Interfaces* **17**, 19512–19525 (2025).
32. Kalita, K. et al. Spontaneous rise of hydrogen microbubbles in interfacial gas evolution reaction. *Small* **20**, 2400849 (2024).
33. Zhang, Y. et al. Programming hydrogen production via controllable emulsification/demulsification in a switchable oil-water system. *ACS Sustain. Chem. Eng.* **7**, 7768–7776 (2019).
34. Ison, E. A., Corbin, R. A. & Abu-Omar, M. M. Hydrogen production from hydrolytic oxidation of organosilanes using a cationic oxorhenium catalyst. *J. Am. Chem. Soc.* **127**, 11938–11939 (2005).
35. Toutov, A. A., Betz, K. N., Haibach, M. C., Romine, A. M. & Grubbs, R. H. Sodium hydroxide catalyzed dehydrocoupling of alcohols with hydrosilanes. *Org. Lett.* **18**, 5776–5779 (2016).
36. Dyett, B. P. & Zhang, X. Accelerated formation of H_2 nanobubbles from a surface nanodroplet reaction. *ACS Nano* **14**, 10944–10953 (2020).
37. Lv, P. et al. Self-propelled detachment upon coalescence of surface bubbles. *Phys. Rev. Lett.* **127**, 235501 (2021).
38. Dogra, P. et al. Binary microdroplets as liquid hydrogen carriers for enhanced hydrogen production. *Chem. Eng. J.* **512**, 162030 (2025).
39. Zhang, X. et al. Propelling microdroplets generated and sustained by liquid–liquid phase separation in confined spaces. *Soft Matter* **17**, 5362–5374 (2021).
40. Foster, P. J. et al. Dissipation and energy propagation across scales in an active cytoskeletal material. *Proc. Natl. Acad. Sci.* **120**, e2207662120 (2023).
41. Antonov, A. P., Musacchio, M., Löwen, H. & Caprini, L. Self-sustained frictional cooling in active matter. *Nat. Commun.* **16**, 7235 (2025).
42. Breoni, D., Kurzthaler, C., Liebchen, B., Löwen, H. & Mandal, S. Giant activity-induced elasticity in entangled polymer solutions. *Nat. Commun.* **16**, 5305 (2025).
43. Sanogo, B., Dogra, P., Kalita, K., Neto, C. & Zhang, X. Interfacial hydrogen evolution reaction from Ouzo-effect-generated bulk

nano/micro droplets of liquid organic hydrogen carriers. *J. Colloid Interface Sci.* **691**, 137346 (2025).

Acknowledgments

The authors thank H.A. Stone and the participants of the workshop celebrating the 80th birthday of Andrea Prosperetti for stimulating discussions. This manuscript was edited for language and clarity with the help of Gemini 3; the authors assume full responsibility for the content.

Author contributions

K.F., B.S., Q.L. and Y.L. contributed equally to this work. X.H.Z. conceived and supervised the project. K.F. performed the experiments, analyzed the data, and compiled the measurements. B.S. and Q.L. conducted additional experiments, interpreted the results, and prepared and revised the manuscript. Y.L. performed the numerical simulations and drafted the corresponding results. D.L. developed the theoretical model, contributed to data interpretation, and revised the manuscript. B.B.-X. assisted with data visualization and revised the manuscript. D.D. co-supervised the project. All authors discussed the results and contributed to the final manuscript.

Funding

X.H.Z. discloses support for the research of this work from the Canada Foundation for Innovation (John R. Evans Leaders Fund) and the Canada Research Chairs Program. This work was also supported by the Natural Sciences and Engineering Research Council of Canada (NSERC) through a Discovery Grant, an Alliance-Alberta Innovates Advance Grant, and Alliance International Catalyst and Collaboration Grants.

Competing interests

The authors declare no competing interests.

Additional information

Supplementary information The online version contains supplementary material available at https://doi.org/10.1038/s41467-026-74223-5.

Correspondence and requests for materials should be addressed to Detlef Lohse, Daosheng Deng or Xuehua Zhang.

Peer review information *Nature Communications* thanks the anonymous reviewers for their contribution to the peer review of this work. A peer review file is available.